PNAS RESEARCH ARTICLE | APPLIED PHYSICAL SCIENCES

How liquid–liquid phase separation induces active spreading

Youchuang Chao[a,1], Olinka Ramírez-Soto[a], Christian Bahr[a], and Stefan Karpitschka[a,1]

Edited by David Weitz, Harvard University, Cambridge, MA; received March 3, 2022; accepted June 13, 2022

The interplay between phase separation and wetting of multicomponent mixtures is ubiquitous in nature and technology and recently gained significant attention across scientific disciplines, due to the discovery of biomolecular condensates. It is well understood that sessile droplets, undergoing phase separation in a static wetting configuration, exhibit microdroplet nucleation at their contact lines, forming an oil ring during later stages. However, very little is known about the dynamic counterpart, when phase separation occurs in a nonequilibrium wetting configuration, i.e., spreading droplets. Here we show that liquid–liquid phase separation strongly couples to the spreading motion of three-phase contact lines. Thus, the classical Cox–Voinov law is not applicable anymore, because phase separation adds an active spreading force beyond the capillary driving. Intriguingly, we observe that spreading starts well before any visible nucleation of microdroplets in the main droplet. Using high-speed ellipsometry, we further demonstrate that the evaporation-induced enrichment, together with surface forces, causes an even earlier nucleation in the wetting precursor film around the droplet, initiating the observed wetting transition. We expect our findings to improve the fundamental understanding of phase separation processes that involve dynamical contact lines and/or surface forces, with implications in a wide range of applications, from oil recovery or inkjet printing to material synthesis and biomolecular condensates.

phase separation | wetting | moving contact line | surface force | multicomponent droplet

Significance

Phase separation plays a central role in many natural and engineering processes, such as cloud formation, biomolecular condensation, and oil recovery. In most situations, phase separation occurs in heterogeneous environments, accompanied by surface wetting. While the scenario for static wetting has been extensively studied, the dynamic counterpart remains largely unexplored. Driving highly mobile droplets of binary mixtures into their miscibility gap, we reveal that liquid–liquid phase separation may cause active spreading, beyond capillarity or gravity-based laws. This motion precedes bulk coarsening and is associated with premature interfacial nucleation, due to evaporative enrichment and surface forces. Such strong coupling between dynamical capillary phenomena and phase separation could be an important building block in nanoscale processing, for instance, on semiconductor surfaces.

Phase separation or demixing of homogeneous liquid mixtures into two or more distinct phases frequently occurs in nature and everyday life and critically impacts a variety of engineering applications (1), such as oil recovery (2), inkjet printing (3), and materials synthesis (4). In most practical situations, phase separation processes occur in heterogeneous environments, i.e., in contact with surfaces, because the interaction with surfaces facilitates nucleation (5). Thus, the interplay of phase separation and wetting is often nontrivial and cannot be ignored (6, 7). For instance, the wettability of rock surfaces can strongly affect the separation efficiency of a crude oil–water mixture for recovering oil from underground reservoirs (2). Even for a single-component liquid, the kinetics of phase transition between different liquid states can be altered by the presence of solid surfaces (8). In addition to technical applications, the coexistence of phase separation and wetting is found in biological settings. A typical example is the protein condensation, a key process for living cells to form membraneless organelles (9, 10), which happens not only in bulk cytoplasm, but frequently on surfaces like the nucleus, microtubuli, and lipid bilayers (11, 12). In the latter case, the wetting properties of biological membranes play an essential role, for instance, in regulating autophagy of the phase-separated compartments (13).

Earlier studies have revealed the physical mechanisms of heterogeneous nucleation, such as the effect of particle sizes and surface properties on the nucleation efficiency (14, 15) or the impact of preferential wetting on spinodal decomposition in binary liquid mixtures (16, 17). Recent work has demonstrated how selective evaporation of sessile droplets in various static wetting configurations modulates nucleation and coarsening processes, e.g., in evaporating ternary Ouzo drops (18, 19). Most of those studies focus on the aspect of static wetting, i.e., pinned three-phase contact-line conditions (18–21). Nevertheless, it remains unclear how the dynamic counterpart, e.g., moving contact lines (22–24), interacts with phase separation, despite its abundance in many natural and industrial scenarios.

Here we explore the interplay between phase separation and wetting dynamics, using droplets of an evaporating, nonideal, binary liquid mixture with a well-defined miscibility gap on completely wetting substrates. We adopt droplets of water and glycol ethers as a model system that exhibits a lower critical solution temperature (LCST) close to room temperature (*SI Appendix*, Fig. S1 and Table S1). In the one-phase region, due to solutal Marangoni flows, the droplet maintains a quasi-stationary, contracted state with a nonzero apparent contact angle θ_{app} and a high mobility, i.e., an unpinned contact line (25–28) (Fig. 1*A*). We then trigger phase separation by driving the droplet into the miscibility

Author affiliations: [a]Dynamics of Complex Fluids, Max Planck Institute for Dynamics and Self-Organization, 37077 Göttingen, Germany

Author contributions: Y.C. and S.K. designed research; Y.C., O.R.-S., and C.B. performed research; Y.C. analyzed data; and Y.C. and S.K. wrote the paper.

The authors declare no competing interest.

This article is a PNAS Direct Submission.

[1]To whom correspondence may be addressed. Email: youchuang.chao@ds.mpg.de or stefan.karpitschka@ds.mpg.de.

This article contains supporting information online at https://www.pnas.org/lookup/suppl/doi:10.1073/pnas.2203510119/-/DCSupplemental.

Published July 22, 2022.

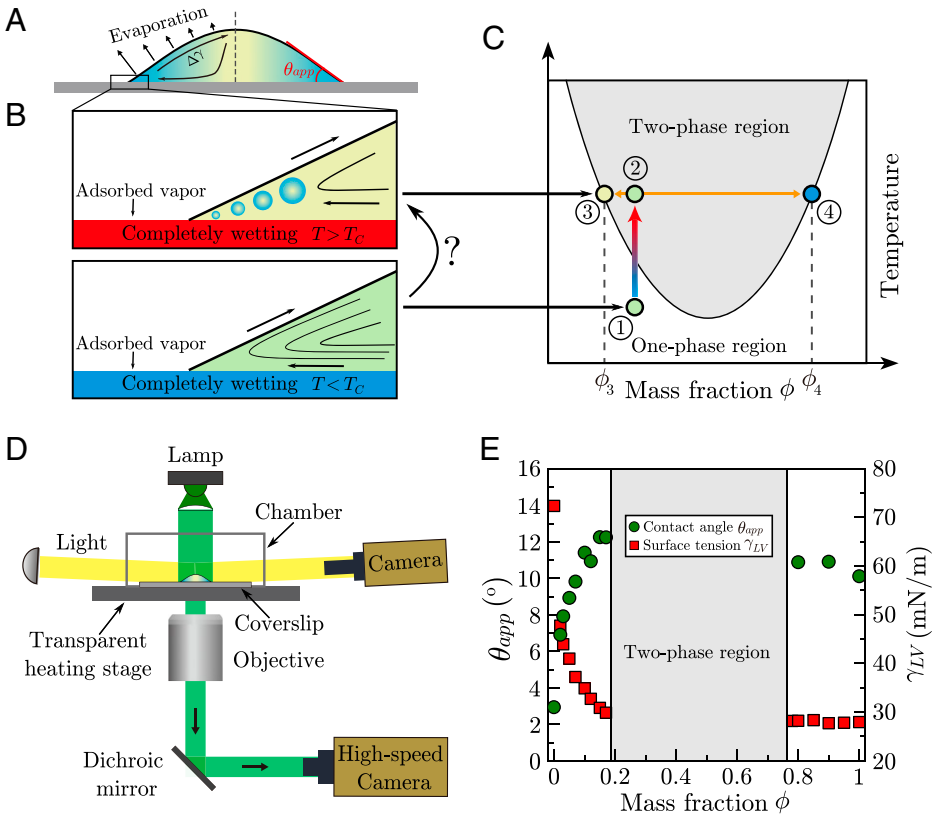

Fig. 1. Experimental system and setup. (*A*) Schematic cross-section of an evaporating binary droplet on completely wetting surfaces, with a nonzero apparent contact angle due to solutal Marangoni flows. (*B*) Zoom-in to the contact-line region before and during phase separation, triggered by heating the substrate. (*C*) Schematic phase diagram of a binary-liquid system with a LCST. Upon heating from the one-phase region 1 to the two-phase region 2, the mixture separates into two phases 3 and 4. (*D*) Schematic of the experimental setup, with simultaneous observation from the side and below. (*E*) Apparent contact angle θ_{app} (green) and surface tension γ_{LV} (red) of the DPnP–water mixture versus DPnP mass fraction ϕ on completely wetting surfaces at $T \sim 20\,^{\circ}\mathrm{C}$.

gap, by heating and/or selective evaporation (Fig. 1 *B* and *C*). Surprisingly, upon liquid–liquid phase separation, we see actively driven droplet spreading. Notably, spreading occurs before any visible nucleation of microdroplets in the main droplet. High-speed ellipsometry reveals an even earlier phase separation in the precursor film around the droplet, evidencing the strong coupling of phase separation and surface wetting, which leads to the observed wetting transition.

Results

Experimental Setup and System. To heat droplets in a precise manner, we built a computer-controlled heating system, which was mounted on top of an inverted microscope (Nikon Ti2E). As substrates, we used precision microscope coverslips (thickness 0.17 mm; VWR) and one-side frosted microscope slides (thickness 0.96 to 1.06 mm; Corning), cleaned by piranha solutions or plasma treatment to generate completely wetting surfaces or by ethanol for partially wetting surfaces. Droplets of initial volumes $\Omega = 0.5$ to 2 µL were deposited onto the substrates and then heated at a controlled rate. Bottom-view and side-view images were simultaneously recorded by a high-speed camera (50 to 500 fps; Phantom VEO 4K-L) on the microscope and a digital camera (27 fps; Point Gray Grasshopper2) attached to a telecentric lens, respectively (Fig. 1 D). We used binary mixtures of water (resistivity 18.2 MΩ · cm; "Milli-Q") and di(propylene glycol) propyl ether (DPnP) ($\geq$ 98.5%; Sigma-Aldrich, mass fraction ϕ), unless stated otherwise (see *Materials and Methods* for experimental details).

Fig. 1*E* shows the apparent contact angle θ_{app} (green) and the surface tension γ_{LV} (red) versus ϕ of our DPnP–water mixture in the one-phase region on completely wetting substrates. However, the apparent contact angles are quasi-statically nonzero: The single-phase water-rich binary mixture exhibits strong Marangoni contraction, whereas the glycol ether-rich mixture shows autophobing (29). What happens when the droplet is now forced into the two-phase region (Fig. 1 *B* and *C*)?

Abrupt Spreading. We begin with investigating the macroscopic dynamics by heating droplets in pinned and unpinned situations, i.e., by partially and completely wetting, respectively. Fig. 2*A* illustrates a typical image sequence of a 1-µL DPnP–water binary droplet with $\phi = 0.1$ heated on a completely wetting substrate. During heating of the substrate, we first observe enhanced contraction (Fig. 2 *A* [0 to 6.5 s] and *B*), owing to the increased selective evaporation and thus intensified Marangoni flows. However, surprisingly, above a certain temperature ($T_C \sim 37\,^{\circ}\mathrm{C}$), a sharp transition into an abrupt spreading motion is observed (Fig. 2 *A* [6.5 to 9.2 s] and *B*). Shortly thereafter, droplet spreading is accompanied by nucleation and growth of DPnP-rich microdroplets (Fig. 2 *A* [9.2 s] and Movie S1). The typical delay from placing the droplet until spreading or phase separation occurs is $\lesssim \mathcal{O}(10\,\mathrm{s})$, much smaller than the timescale of depletion of the volatile component [$\sim \mathcal{O}(100\,\mathrm{s})$], so the volumetric effect of evaporation is negligible. A qualitatively similar behavior is observed without heating, once water has depleted sufficiently from the droplet to trigger phase separation (*SI Appendix*, Fig. S6).

In contrast, droplets of DPnP–water mixtures on partially wetting surfaces (ethanol-cleaned coverslips) phase separate in

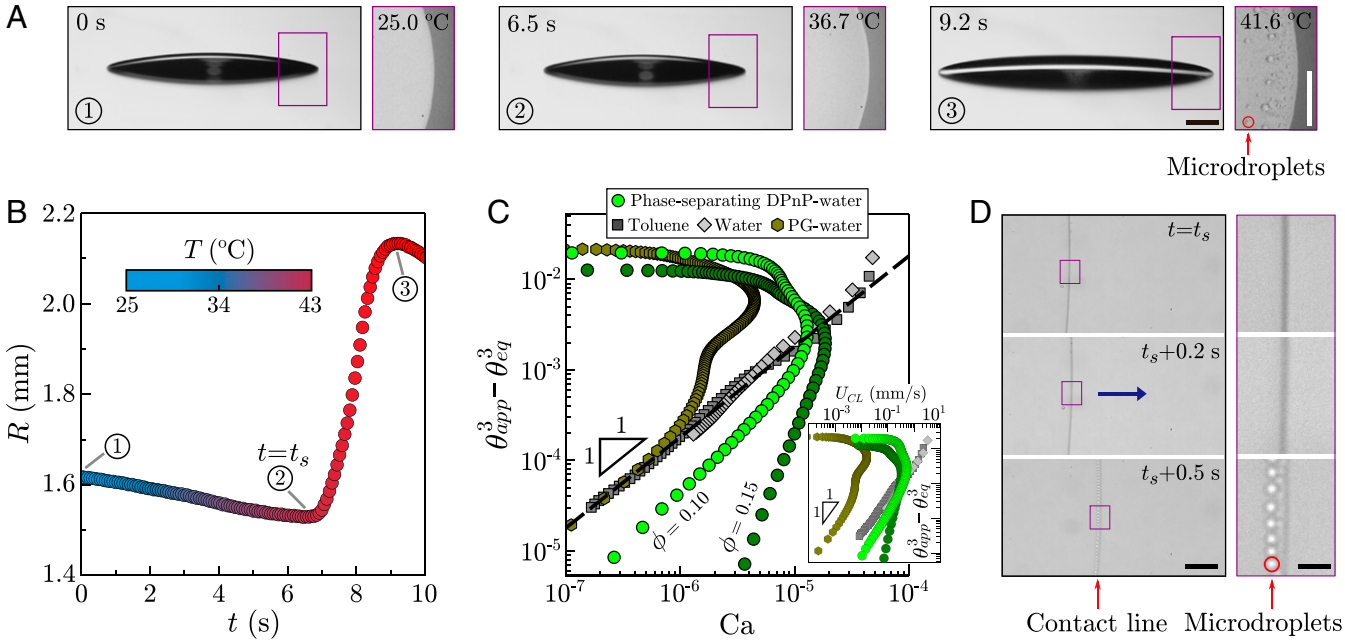

Fig. 2. Active spreading of a 1-μL phase-separating DPnP–water droplet on a substrate heated at ∼1.8 °C s^{-1}. (*A*, *1–3*) Image sequence of the side aspect of the droplet ($\phi = 0.1$) (*Left*) together with the bottom view of the contact-line region (*Right*). (Scale bars, 0.25 mm.) (*B*) Droplet radius *R* versus time *t* and temperature *T* as color code. t_s marks the onset of spreading. (*C*) $\theta_{app}^3 - \theta_{eq}^3$ versus the capillary number Ca for phase-separating DPnP–water mixtures ($\phi = 0.1$ and 0.15, light and dark green, respectively), compared to simple fluids toluene and water (dark and light gray, respectively) and the fully miscible PG–water mixture ($\phi = 0.5$, dark yellow). Simple fluids follow the Cox–Voinov law (Eq. **1**), collapsing onto a single line of slope 1 (dashed line); non–phase-separating PG–water spreads slower, following the Cox–Voinov law only in the very end; phase-separating DPnP–water spreads significantly faster than miscible or pure liquids. *Inset* shows data as a function of the physical U_{CL} (*SI Appendix*, Fig. S4). (*D*) High-resolution images of the contact-line region. Spreading (direction indicated by the arrow) starts first, and microdroplets appear later. (Scale bars, 50 μm [*Left*] and 10 μm [*Right*].)

their bulk as temperature increases, without any apparent change of their wetting behavior (Movie S2). This latter scenario is consistent with previous studies on the evaporation-driven phase separation (segregation) of ternary (18, 19) or binary (30, 31) droplets on partially wetting surfaces and/or subject to contact-line pinning.

As a control experiment without phase separation, for instance to clarify the impact of thermal (32, 33) or solutal (34) Marangoni convection, we replace DPnP with a glycol of similar surface activity, propylene glycol (PG) ($\phi = 0.5$; Sigma-Aldrich, ≥ 99.5%) (35, 36). Note that PG and water are well miscible, meaning that their mixture does not exhibit liquid–liquid phase separation throughout our experimental conditions. In this case, we observe enhanced contraction during all of the heating phase. Only much later, due to the gradual depletion of water from the droplet, the Marangoni flows decay and hence the droplet spreads slowly (Movie S3 and *SI Appendix*, Fig. S2) (25, 36).

Impact of Phase Separation on Spreading. For pure liquids, the dynamics of advancing contact lines follow the classical Cox–Voinov law (37, 38)

$$\theta_{app}^3 - \theta_{eq}^3 = 9\,\mathrm{Ca}\ln\left(\alpha\,\frac{l_o}{l_i}\right), \qquad [1]$$

where θ_{app} and θ_{eq} denote the dynamical apparent contact angle and the equilibrium contact angle, respectively. $\mathrm{Ca} = \mu U_{CL}/\gamma_{LV}$ is the capillary number, μ the dynamic viscosity, and U_{CL} the speed of the moving contact line. α is a nonuniversal numerical constant, and l_o and l_i indicate an outer (macroscopic) and an inner (microscopic) length (23, 39). Fig. 2*C* shows the dependence of $\theta_{app}^3 - \theta_{eq}^3$ on Ca and, in Fig. 2 *C*, *Inset* on U_{CL}, for phase-separating DPnP–water ($\phi = 0.1$, light green and $\phi = 0.15$, dark green), toluene (dark gray), water (light gray), and PG–water ($\phi = 0.5$, dark yellow) droplets, respectively. Here, for the DPnP–water mixtures, toluene, water, and the PG–water mixture, θ_{eq}s are ∼6.1° ($\phi = 0.1$), ∼6.3° ($\phi = 0.15$), ∼5.5°, ∼2.7°, and ∼4.2°, respectively. As expected, experimental data of toluene and water collapse onto a master curve (black dashed line), following the Cox–Voinov law (Eq. 1). For the binary mixtures, we observe a deviation from the Cox–Voinov law: PG–water droplets spread slower, due to a gradually decaying Marangoni contraction (25, 36), whereas, surprisingly, the phase-separating binary droplets spread much faster, evidencing a direct coupling of phase separation to the spreading process, in the opposite direction compared to the Marangoni flows in the miscible region. Besides larger capillary numbers, phase separation generates exponents greater than 1, increasing with the glycol–ether mass fraction (Fig. 2*C*). Thus, phase separation accelerates spreading.

Of course, there is no single well-defined capillary velocity, $U_{cap} = \gamma_{LV}/\mu$ for a droplet with ongoing phase separation, since in general, the two phases exhibit different viscosities, and an emulsion may, on top, show non-Newtonian behavior (40). Nonetheless, it is instructive to nondimensionalize the contact line velocity U_{CL} with a characteristic value that is representative for the given situation. We measure surface tensions and viscosities in water-rich ($\phi = 0.1$ and 0.15) and the corresponding DPnP-rich one-phase regions at the temperature that droplet starts spreading, obtaining for $\phi = 0.1$ capillary velocities ∼40 m/s and ∼6.5 m/s, respectively, and for $\phi = 0.15$ capillary velocities ∼18 m/s and ∼4.2 m/s, respectively. In Fig. 2*C*, we use the value for the water-rich phase, which corresponds to the initial condition for the abrupt spreading and the volumetrically dominating phase throughout this process. The presence of glycol ether-rich microdroplets would increase the apparent viscosity (*SI Appendix*, Fig. S3). Therefore, the curves are a lower bound

for the actual capillary number; In SI Appendix, we also depict the range of possible capillary numbers (*SI Appendix*, Fig. S4). Instead, for the PG–water mixture, we use the viscosity of pure PG, which is appropriate for the final spreading and gives an upper bound for the capillary number at earlier times (Fig. 2 *C* and *SI Appendix*, Fig. S4).

To identify phase separation near the contact line, we further record bright-field images at higher spatial resolution at ×40 magnification (numerical aperture 0.60). As previously observed for pinned droplets (18), microdroplets nucleate and grow at the contact-line region (Fig. 2 *D* and Movie S4). However, microdroplets appear only around 0.44 s after the onset of contact-line motion (*SI Appendix*, Fig. S5). We also confirm the generality of this phenomenon in our experimental system, using a wide range of heating rates (0.9 to 0.3 °C/s) and different mass fractions of DPnP ($\phi =$ 0.05, 0.15), as well as binary mixtures made of water and different glycol ethers [tri(propylene glycol) propyl ether (TPnP) and di(propylene glycol) butyl ether (DPnB)] (*SI Appendix*, Fig. S6). Visible coarsening is quantified in the images by the average pixel-wise absolute deviation of the intensity in the contact-line region from a reference image, a signal that grows rapidly once nuclei reach the resolution limit (∼400 nm) (*SI Appendix*, Figs. S5 and S6). This suggests that the spreading-relevant phase change occurs before visible coarsening (Fig. 3 *A* and *B*), either at distances below the optical resolution (∼400 nm) to the contact line or in the precursor film outside the droplet. In the precursor, which is formed by vapor adsorption, surface forces may also impact composition and phase behavior.

Phase Separation in the Precursor Film. Based on the above observations (Fig. 2*D*), we hypothesize that, besides the effect of evaporative enrichment (18), surface forces could promote an earlier phase change within the precursor film. In our system, surface forces are mainly due to van der Waals interactions across the three phases, air/liquid/substrate, which can be quantified in the form of a disjoining pressure

$$\Pi(h) = \frac{A}{6\pi h^3}, \qquad [2]$$

where $A \sim -10^{-20}$J, the Hamaker constant (41) (adopting the sign convention from ref. 23). For Eq. **2** to attain values significant to thermodynamic equilibrium (on the order of atmospheric pressure), $h \sim \mathcal{O}(1\,\mathrm{nm})$ is required, the typical thickness of a precursor film (42). For complete wetting conditions, van der Waals forces are repulsive, i.e., $\Pi(h) < 0$, giving rise to a reduced pressure that tends to thicken the precursor film. This reduced pressure also provides the equilibrium of the precursor with the undersaturated vapor above it (43). Therefore, given the ambient humidity and the vapor pressures of water and glycol ether, we expect a monotonously increasing water fraction in the precursor away from the droplet. However, composition-dependent surface forces might alter the equilibrium (44, 45).

To investigate phase separation in the precursor film, we use high-speed in situ ellipsometry, which allows for detecting subtle variations of thickness or refractive index in molecularly thin films (42) (*Materials and Methods* and *SI Appendix*, Fig. S7). Fig. 3 *C–F* shows the ellipsometric angle Δ (symbols) as a function of time relative to the onset of spreading, $t - t_s$, at three different heating rates (0.5, 0.25, and 0 °C/min, Fig. 3*C–E*, respectively; 0 °C/min, Fig. 3*F*). Note that phase separation also happens at constant temperatures above the LCST, due to selective evaporation (Fig. 3 *E* and *F*). For Fig. 3 *C–E*, the measurement spot is located at a distance $d \approx 0.5$ mm away from the macroscopic contact line (Fig. 3 *A* and *SI Appendix*, Fig. S7). For Fig. 3*F*, the distance is around 5 mm.

Long before the onset of spreading ($t - t_s \lesssim -20$ s), we find a fluctuating Δ. We attribute this to the fluctuations in the evaporation/condensation equilibrium between the vapor and the hydrophilic surface (29), which are also observed when placing a pendant droplet above a fully wetting substrate (*SI Appendix*, Fig. S8). Around $t - t_s \sim -20$ s, we observe an abrupt increase of Δ, which is small but distinguishable from noise and reproduced in all repetitions of these experiments. Another ∼5 to 10 s later, we see a rapid decrease of Δ (Fig. 3 *C–E*). On the contrary,

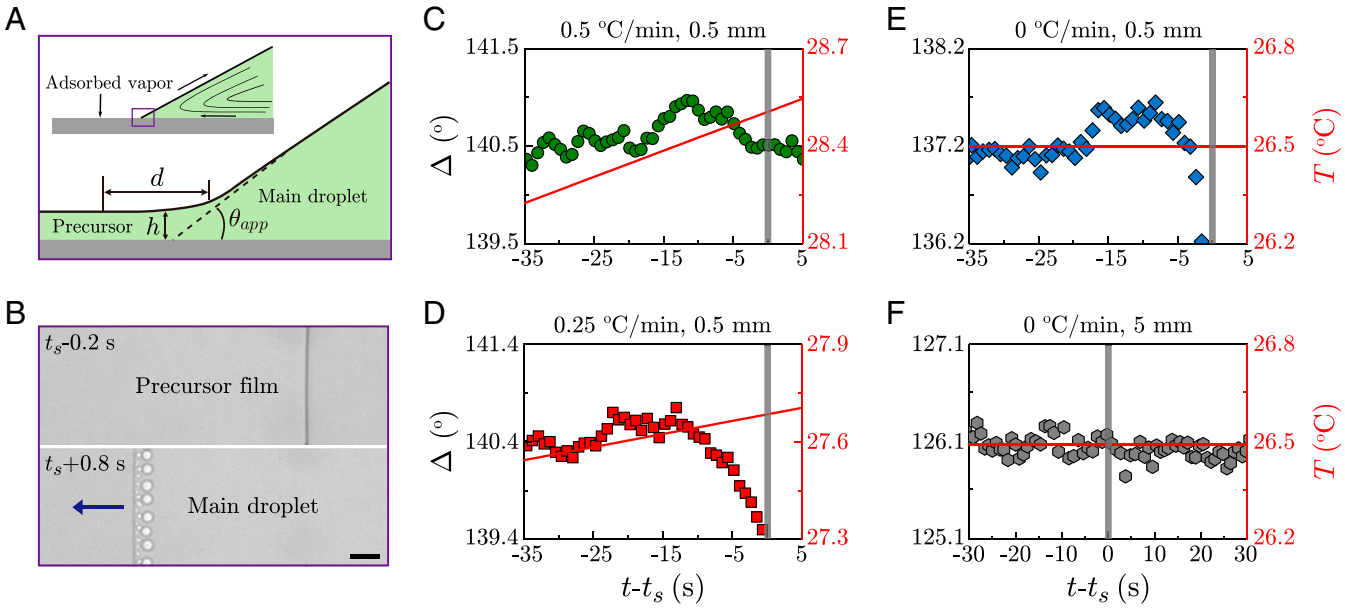

Fig. 3. Analysis of the precursor film around the main droplet. (*A*) Schematic cross-section of the micro/nanoscopic contact-line region. *h* and *d* denote film thickness and distance to the contact line, respectively. (*B*) High-resolution images of the contact-line region 0.2 s before and 0.8 s after the onset of spreading at t_s. (Scale bar, 20 μm.) (*C–F*) Ellipsometric angle Δ (symbols) measured at distance *d* to the contact line and temperature *T* (red lines) vs. $t - t_s$: three different heating rates of 0.5, 0.25, and 0 °C · min^{-1} at $d \sim 0.5$ mm (*C–E*, respectively) and 0 °C · min^{-1} at $d \sim 5$ mm (*F*). For constant $T \sim 26.5$ °C (*E* and *F*), phase separation is triggered by selective evaporation. Vertical (gray) lines are a guide to the eye.

at a large distance to the droplet (comparable to its radius), we do not observe any measurable change in the ellipsometric signal (Fig. 3*F*).

Our results clearly evidence the existence of a compositional or morphological variation in the precursor close to the main droplet, ahead of any macroscopically visible effect, most probably caused by earlier nucleation in the precursor film. This variation is sensitive to the distance d from the macroscopic contact line. The precursor film is, due to its microscopic thickness, always very close to equilibrium with the vapor above it, and the vapor density around an evaporating droplet decays $\sim 1/d$ (43). Due to water evaporation, DPnP enriches near the contact line in the droplet, which might affect also the precursor composition near the droplet. However, far from the contact line, the less volatile DPnP molecules are outnumbered by the more volatile water molecules, which are abundant in the atmosphere due to the natural humidity. As such, the phase boundary is hardly ever reached far from the droplet, even though the precursor film becomes much thinner (46). We note here that no visible increase of Δ could be observed for large heating rates $\gtrsim 1.2\,^{\circ}$C/min (*SI Appendix*, Fig. S9), for which the effect is probably beyond the sampling period (~ 0.8 s) of our ellipsometer.

Preferential Wetting in the Two-Phase Region. Finally, to rationalize on which surface (solid–liquid or liquid–vapor) nucleation first emerges, we test the wetting preference of water-rich and glycol ether-rich droplets on either surface. Here, mutually saturated water-rich and DPnP-rich phases are extracted from bottom and top phases of a well-equilibrated DPnP–water mixture at a 1:1 mass ratio, respectively (*Materials and Methods*). A water-rich droplet in a DPnP-rich outer phase preferentially wets the clean glass, spreading to small contact angles (green; Fig. 4, *Inset A*). Exchanging droplet and outer phases, the contact angle remains large, close to 180° (red; Fig. 4, *Inset B*). In both cases, buoyancy is used to push the droplet against the substrate, which is thus located above the droplet in the latter case. The opposite behavior is observed at the liquid–air interface, where the DPnP-rich phase spreads along the free surface (blue; Fig. 4, *Inset C*; and see also *SI Appendix*, Fig. S10 for additional cases on the wettability test).

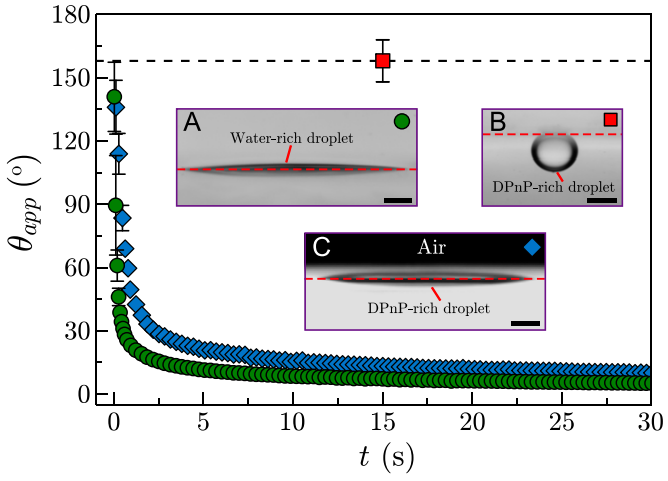

Fig. 4. Preferential wetting of the two mutually saturated liquid phases at the interface with glass and air: contact angle vs. time (main panel) and side aspects of the immersed droplets (*Insets*). (*Inset A*) Water-rich droplet spreading on hydrophilic glass in a DPnP-rich ambient phase (green circles). (*Inset B*) DPnP-rich droplet dewetted from hydrophilic glass (located above the droplet to have buoyancy pushing the drop against the glass) in a water-rich ambient phase (red square). (*Inset C*) DPnP-rich droplet spreading at the free surface of a water-rich ambient phase (blue diamonds). Red dashed lines represent the surface location. (Scale bars, 5 mm.)

These observations suggest that the glycol ether-rich phase faces a lower energy barrier for nucleation at the liquid–air interface, compared to the bulk of the main droplet or at the substrate surface (5, 47).

Although these results cannot readily be transferred to the precursor region, where the presence of three phases in close proximity leads to strong surface forces that may alter wetting preferences, they render a "leaking out" (48) of DPnP rather unlikely. Instead, an increased water fraction in the precursor film would be expected. Yet, there the phase change appears well before the spreading or the visible microdroplet nucleation.

Discussion and Conclusions

In contrast to binary or ternary droplets on partially wetting surfaces with pinned contact lines (18, 19, 30, 31, 49–54), here we report unexpected spreading of phase-separating binary-mixture droplets on fully wetting surfaces with free contact lines. Interestingly, we find that Cox–Voinov law is outrun by such droplets, because phase separation accelerates the contact-line motion. A closer inspection of droplet edges reveals that visible coarsening in the main droplet occurs later than the advancing motion of the contact line. Ellipsometric measurements detect phase separation even earlier in the precursor film, $\sim 500\,\mu$m outside the droplet, where the concentration of glycol ether should already decay, but surface forces are strong. We demonstrate that the nucleating (glycol ether-rich) phase has a strong wetting preference for the liquid–air interface. We therefore conclude that, when the binary mixture is pushed into the two-phase region, the combination of enrichment and surface forces causes the onset of phase separation (55) in nanoscopic proximity to the contact line. It is this earlier phase separation that drives the contracted droplet away from its quasi-stationary state and changes the force balance at the three-phase contact line (25, 56), thus initiating the active spreading.

It is worth noting that no apparent spreading motion can be seen when starting with droplets on the glycol ether-rich side of the miscible region, such as DPnP with $\phi = 0.8$ (Movie S5). Water evaporation at the free surface drives the composition farther away from the phase boundary, and thus phase separation starts near the substrate and the center of the droplet where it does not affect wetting. Further, the molecular autophobicity of glycol ethers on hydrophilic glass may prevent the droplet from spreading over its own adsorbed film, causing contact-line pinning (46).

To summarize, we have demonstrated that the strong coupling between phase separation, moving contact lines, evaporation-induced enrichment, and wetting precursors results in enhanced spreading on high-energy surfaces, well beyond the capillarity–dissipation balance of Cox–Voinov spreading. Our work shows experimentally the crucial role of phase separation and mobile contact lines in dynamic multiphase systems, motivating future studies to reveal the molecular processes and build a theoretical understanding of these observations (57). Moreover, the development of numerical frameworks capable of including long-range interactions, phase separation, and wetting would be especially helpful in quantifying these complex "multiscale" phenomena (58–60). We expect these phenomena to be general to binary systems where the criteria of complete wetting (i.e., absence of autophobing), miscibility gap, enrichment, and surface tension contrast are met. More importantly, this renders the findings relevant well beyond droplet studies, for instance, to advance our fundamental understanding of active wetting transitions in tissue morphogenesis (61), phase separation nanoengineering applications (62–64), or liquid–liquid phase separation dynamics in cell biology (65–67).

Materials and Methods

Preparation of the Substrates. Microscope coverslips (24 × 24 mm, thickness 0.17 mm; VWR) or one-side–frosted microscope slides (75 × 25 mm, thickness 0.96 to 1.06 mm; Corning) were treated with ethanol, plasma, or piranha solutions before use. For ethanol cleaning, substrates were sonicated in ethanol in the ultrasonic bath for 20 min and then stored in fresh water (resistivity 18.2 MΩ · cm; Milli-Q). For plasma cleaning, substrates were sonicated in an acetone solution for 15 min, followed by an ethanol solution for 15 min, and then rinsed with water, dried in the oven, and finally treated with oxygen plasma (Harrick Plasma) for ∼3 min. For piranha cleaning, substrates were treated in piranha solutions (hydrogen peroxide 30% and sulfuric acid 95%; VWR, mixture 1:3 by volume) for 20 min. Then, the substrates were rinsed with fresh water five times, sonicated in hot water (∼80 °C) for 10 min, and stored in fresh water. The ethanol- and piranha-cleaned substrates were used on the day of preparation and dried with a nitrogen drying gun in a laminar flow hood immediately before each measurement. The plasma-cleaned substrate was used immediately after preparation.

Preparation of the Binary Mixtures. For binary solutions, we prepared a mixture consisting of water (Milli-Q) and one of the following glycol ethers: DPnP (≥98.5%), TPnP (97%), and DPnB (≥98.5%) or a typical glycol: PG (≥99.5%). For spreading of pure liquids, we use water and toluene (≥99.9%). All chemicals were purchased from Sigma-Aldrich.

Preparation of Two Mutually Saturated Phases. The immiscible DPnP–water solution was prepared by first mixing DPnP and water in a mass ratio of 1:1. The well-mixed solution was then centrifuged in a laboratory centrifuge (Centrifuge 5804R; Eppendorf) at 4,000 rpm for 2 h and allowed to phase separate for more than 48 h. Finally, the two mutually saturated phases, namely, water-rich and DPnP-rich solutions, were collected from bottom and top layers of the well-equilibrated mixture, respectively.

Measurements of Liquid Viscosity, Surface Tension, and Contact Angle. The viscosity μ was measured by a temperature-controlled rheometer (MCR 502; Anton Paar), and the surface tension γ_{LV} was measured with a goniometer (OCA 20; DataPhysics Instruments) using the pendant drop method. For each mixture, at least 10 droplets were measured and analyzed to obtain the surface tension, with an average error of 0.16 mN/m. The static apparent contact angle θ_{app} (Fig. 1*E*) was measured with this goniometer, using the sessile drop method.

Observation of the Main Droplet. The recording of the main droplet was performed in a custom-built chamber (∼10 × 10 × 5 cm), mounted on the top of an inverted (epifluorescence) microscope (Nikon Ti2E). A computer-controlled heating system was built into the chamber, allowing a well-defined temperature and heating rate at the substrate. The heating system was composed of a transparent indium tin oxide (ITO) glass (28 × 28 mm, thickness 0.7 mm; Praezisions Glas & Optik GmbH), a custom-built proportional-integral-derivative (PID) controller, and a Python-based controlling interface. To improve the accuracy of the temperature measurements, the substrate surface was monitored during test heating cycles by an infrared thermal imaging camera (Laserliner). The temperature deviation among different cycles was less than 0.5 °C in our experimental condition. Droplets composed of mixtures of water and a glycol ether or PG, or a pure liquid, with initial volumes $\Omega = 0.5$ to 2 μL, were gently deposited onto the cleaned coverslip with a glass syringe (Hamilton GasTight). Afterward, droplet behavior was observed simultaneously by two cameras: one high-speed camera (50 to 500 fps; Phantom VEO 4K-L) for the bottom-view recording and another digital camera (27 fps; Point Gray Grasshopper2) attached to a macrolens (1.0×, working distance. 62.2 mm; Thorlabs Bi-Telecentric lens) with a collimated light source for the side-view recording (Fig. 1*D*) (68). The bright-field microscopy was performed with either a ×2 Plan Apo objective for observing the whole droplet or a ×40 Plan Fluor objective (numerical aperture 0.60) for observing the contact-line region. The relative humidity and the ambient temperature were stable during experiments, $(30 \pm 5)\%$ and (21 ± 1)°C, respectively. All images were analyzed by custom-made MATLAB codes and/or the open-source software IMAGEJ. The dynamical apparent contact angle θ_{app} (Fig. 2*C*) was obtained from side-view images as $\theta_{app} \simeq 2h_0/R$, where h_0 and R are the maximal height and the foot radius of the droplet, respectively (68).

On-Site Ellipsometric Measurements of the Precursor Film. The variation of precursor film was detected in separate experiments using a high-speed phase-modulated ellipsometer (NeHe laser beam, diameter 0.63 mm, wavelength $\lambda = 633$ nm, sampling period ∼0.8 s) (69). To regulate the substrate temperature, the ellipsometer was equipped with a temperature controller (Eurotherm), which was sampled by a thermal sensor. Furthermore, to minimize the light reflection from the bottom side of the glass substrates, one-side–frosted microscope slides instead of coverslips were applied, and half parts of them were untreated to fix the droplet during measurements. The angle of incidence α_i was adjusted so that the value of ellipsometric angle Δ was near 135°. Typically, low heating rates ($\lesssim$1.2 °C/min) were applied to efficiently capture the fast dynamics of the precursor film, and additionally, droplets with large size $\Omega = 5$ to 10 μL were adopted to reduce the evaporation-induced volume shrinkage. During ellipsometric measurements, the main droplet was simultaneously recorded by a camera (10 fps; Point Gray Grasshopper2) from the top view, with a green light ($\lambda = 550$ nm; KL 1500 LCD) as illumination from the side (*SI Appendix*, Fig. S7). Here, the green light was applied to avoid its interference with the HeNe laser light. Under this condition, the value of Δ was assumed to be most sensitive to the variation inside the precursor film. Measurements were also performed in an atmospheric control chamber to minimize external disturbances in the vapor field due to ambient air currents. For all experiments, each measurement began when the deposited droplet reached a steady state (∼1 to 3 min). During this period, droplets were assumed to form an effective θ_{app} as well as to develop a stable precursor film.

Data Availability. All study data are included in this article and/or *SI Appendix*.

ACKNOWLEDGMENTS. We acknowledge financial support from the Max Planck–University of Twente Center for Complex Fluid Dynamics. Y.C. acknowledges support through an Alexander von Humboldt Fellowship. We also thank J. Chateau, L. D. Rodriguez, A. Barthel, W. Keiderling, K. Hantke, and H. Jeon for assistance with the experiments.

1. D. Lohse, X. Zhang, Physicochemical hydrodynamics of droplets out of equilibrium. *Nat. Rev. Phys.* **2**, 426–443 (2020).
2. A. Muggeridge *et al.*, Recovery rates, enhanced oil recovery and technological limits. *Philos. Trans. R. Soc. Math. Phys. Eng. Sci.* **372**, 20120320 (2013).
3. Y. Xia, R. H. Friend, Controlled phase separation of polyfluorene blends via inkjet printing. *Macromolecules* **38**, 6466–6471 (2005).
4. Y. Chao, H. C. Shum, Emerging aqueous two-phase systems: From fundamentals of interfaces to biomedical applications. *Chem. Soc. Rev.* **49**, 114–142 (2020).
5. D. Turnbull, Kinetics of heterogeneous nucleation. *J. Chem. Phys.* **18**, 198–203 (1950).
6. L. D. Gelb, K. Gubbins, R. Radhakrishnan, M. Sliwinska-Bartkowiak, Phase separation in confined systems. *Rep. Prog. Phys.* **62**, 1573 (1999).
7. H. Tanaka, Interplay between wetting and phase separation in binary fluid mixtures: Roles of hydrodynamics. *J. Phys. Condens. Matter* **13**, 4637 (2001).
8. K. Murata, H. Tanaka, Surface-wetting effects on the liquid-liquid transition of a single-component molecular liquid. *Nat. Commun.* **1**, 16 (2010).
9. S. F. Banani, H. O. Lee, A. A. Hyman, M. K. Rosen, Biomolecular condensates: Organizers of cellular biochemistry. *Nat. Rev. Mol. Cell Biol.* **18**, 285–298 (2017).
10. Y. Shin, C. P. Brangwynne, Liquid phase condensation in cell physiology and disease. *Science* **357**, eaaf4382 (2017).
11. C. P. Brangwynne, P. Tompa, R. V. Pappu, Polymer physics of intracellular phase transitions. *Nat. Phys.* **11**, 899–904 (2015).
12. J. A. Ditlev, Membrane-associated phase separation: Organization and function emerge from a two-dimensional milieu. *J. Mol. Cell Biol.* **3**, mjab010 (2021).
13. J. Agudo-Canalejo *et al.*, Wetting regulates autophagy of phase-separated compartments and the cytosol. *Nature* **591**, 142–146 (2021).
14. N. H. Fletcher, Size effect in heterogeneous nucleation. *J. Chem. Phys.* **29**, 572–576 (1958).
15. B. J. Kim *et al.*, Kinetics of individual nucleation events observed in nanoscale vapor-liquid-solid growth. *Science* **322**, 1070–1073 (2008).
16. P. Guenoun, D. Beysens, M. Robert, Dynamics of wetting and phase separation. *Phys. Rev. Lett.* **65**, 2406–2409 (1990).
17. R. A. Jones, L. J. Norton, E. J. Kramer, F. S. Bates, P. Wiltzius, Surface-directed spinodal decomposition. *Phys. Rev. Lett.* **66**, 1326–1329 (1991).
18. H. Tan *et al.*, Evaporation-triggered microdroplet nucleation and the four life phases of an evaporating Ouzo drop. *Proc. Natl. Acad. Sci. U.S.A.* **113**, 8642–8647 (2016).
19. H. Tan *et al.*, Self-wrapping of an ouzo drop induced by evaporation on a superamphiphobic surface. *Soft Matter* **13**, 2749–2759 (2017).
20. Y. Li, R. Lipowsky, R. Dimova, Membrane nanotubes induced by aqueous phase separation and stabilized by spontaneous curvature. *Proc. Natl. Acad. Sci. U.S.A.* **108**, 4731–4736 (2011).

21. K. E. Jensen *et al.*, Wetting and phase separation in soft adhesion. *Proc. Natl. Acad. Sci. U.S.A.* **112**, 14490–14494 (2015).
22. D. Bonn, J. Eggers, J. Indekeu, J. Meunier, E. Rolley, Wetting and spreading. *Rev. Mod. Phys.* **81**, 739 (2009).
23. J. H. Snoeijer, B. Andreotti, Moving contact lines: Scales, regimes, and dynamical transitions. *Annu. Rev. Fluid Mech.* **45**, 269–292 (2013).
24. H. Benabdelhalim, D. Brutin, Phase separation during blood spreading. *Sci. Rep.* **11**, 11688 (2021).
25. N. J. Cira, A. Benusiglio, M. Prakash, Vapour-mediated sensing and motility in two-component droplets. *Nature* **519**, 446–450 (2015).
26. R. Malinowski, I. P. Parkin, G. Volpe, Nonmonotonic contactless manipulation of binary droplets via sensing of localized vapor sources on pristine substrates. *Sci. Adv.* **6**, eaba3636 (2020).
27. A. Molina, S. Kumar, S. Karpitschka, M. Prakash, Droplet tilings for rapid exploration of spatially constrained many-body systems. *Proc. Natl. Acad. Sci. U.S.A.* **118**, e2020014118 (2021).
28. M. Wu, M. Doi, X. Man, The contact angle of an evaporating droplet of a binary solution on a super wetting surface. *Soft Matter* **17**, 7932–7939 (2021).
29. M. A. Hack *et al.*, Wetting of two-component drops: Marangoni contraction versus autophobing. *Langmuir* **37**, 3605–3611 (2021).
30. Y. Li *et al.*, Evaporation-triggered segregation of sessile binary droplets. *Phys. Rev. Lett.* **120**, 224501 (2018).
31. H. Kim, H. A. Stone, Direct measurement of selective evaporation of binary mixture droplets by dissolving materials. *J. Fluid Mech.* **850**, 769–783 (2018).
32. P. Gurrala, P. Katre, S. Balusamy, S. Banerjee, K. C. Sahu, Evaporation of ethanol-water sessile droplet of different compositions at an elevated substrate temperature. *Int. J. Heat Mass Transf.* **145**, 118770 (2019).
33. A. Williams *et al.*, Spreading and retraction dynamics of sessile evaporating droplets comprising volatile binary mixtures. *J. Fluid Mech.* **907**, A22 (2021).
34. S. K. Parimalanathan, S. Dehaeck, A. Rednikov, P. Colinet, Controlling the wetting and evaporation dynamics of non-ideal volatile binary solutions. *J. Colloid Interface Sci.* **592**, 319–328 (2021).
35. S. Karpitschka, F. Liebig, H. Riegler, Marangoni contraction of evaporating sessile droplets of binary mixtures. *Langmuir* **33**, 4682–4687 (2017).
36. J. Charlier, A. Rednikov, S. Dehaeck, P. Colinet, D. Terwagne, Water–propylene glycol sessile droplet shapes and migration: Marangoni mixing and separation of scales. *J. Fluid Mech.* **933**, A45 (2022).
37. R. Cox, The dynamics of the spreading of liquids on a solid surface. Part 1. Viscous flow. *J. Fluid Mech.* **168**, 169–194 (1986).
38. O. Voinov, Hydrodynamics of wetting. *Fluid Dyn.* **11**, 714–721 (1976).
39. J. Eggers, H. A. Stone, Characteristic lengths at moving contact lines for a perfectly wetting fluid: The influence of speed on the dynamic contact angle. *J. Fluid Mech.* **505**, 309–321 (2004).
40. S. R. Derkach, Rheology of emulsions. *Adv. Colloid Interface Sci.* **151**, 1–23 (2009).
41. J. N. Israelachvili, *Intermolecular and Surface Forces* (Academic Press, 2011).
42. M. N. Popescu, G. Oshanin, S. Dietrich, A. M. Cazabat, Precursor films in wetting phenomena. *J. Phys. Condens. Matter* **24**, 243102 (2012).
43. J. Eggers, L. M. Pismen, Nonlocal description of evaporating drops. *Phys. Fluids* **22**, 112101 (2010).
44. J. W. Gibbs, On the equilibrium of heterogeneous substances. *Trans. Conn. Acad. Arts Sci.* **3**, 108 (1876).
45. J. Wenzel, U. Limbach, G. Bresonik, G. Schneider, Kinetics of phase separation in binary liquid mixtures. *J. Phys. Chem.* **84**, 1991–1995 (1980).
46. V. Novotny, A. Marmur, Wetting autophobicity. *J. Colloid Interface Sci.* **145**, 355–361 (1991).
47. X. Liu, Heterogeneous nucleation or homogeneous nucleation? *J. Chem. Phys.* **112**, 9949–9955 (2000).
48. F. Brochard-Wyart, R. Fondecave, M. Boudoussier, Wetting of antagonist mixtures: The 'leak out' transition. *Int. J. Eng. Sci.* **38**, 1033–1047 (2000).
49. J. R. Christy, Y. Hamamoto, K. Sefiane, Flow transition within an evaporating binary mixture sessile drop. *Phys. Rev. Lett.* **106**, 205701 (2011).
50. H. Kim *et al.*, Controlled uniform coating from the interplay of Marangoni flows and surface-adsorbed macromolecules. *Phys. Rev. Lett.* **116**, 124501 (2016).
51. A. M. J. Edwards *et al.*, Density-driven flows in evaporating binary liquid droplets. *Phys. Rev. Lett.* **121**, 184501 (2018).
52. Y. Li *et al.*, Gravitational effect in evaporating binary microdroplets. *Phys. Rev. Lett.* **122**, 114501 (2019).
53. B. U. Moon *et al.*, Evaporation-driven water-in-water droplet formation. *Langmuir* **36**, 14333–14341 (2020).
54. W. Guo *et al.*, Non-associative phase separation in an evaporating droplet as a model for prebiotic compartmentalization. *Nat. Commun.* **12**, 3194 (2021).
55. H. Sadafi *et al.*, Evaporation induced demixing in binary sessile drops. *Colloids Surf. A Physicochem. Eng. Asp.* **602**, 125052 (2020).
56. A. Benusiglio, N. J. Cira, M. Prakash, Two-component Marangoni-contracted droplets: Friction and shape. *Soft Matter* **14**, 7724–7730 (2018).
57. U. Thiele, D. V. Todorova, H. Lopez, Gradient dynamics description for films of mixtures and suspensions: Dewetting triggered by coupled film height and concentration fluctuations. *Phys. Rev. Lett.* **111**, 117801 (2013).
58. D. M. Anderson, G. B. McFadden, A. A. Wheeler, Diffuse-interface methods in fluid mechanics. *Annu. Rev. Fluid Mech.* **30**, 139–165 (1998).
59. C. Diddens *et al.*, Evaporating pure, binary and ternary droplets: Thermal effects and axial symmetry breaking. *J. Fluid Mech.* **823**, 470–497 (2017).
60. E. Vidal-Henriquez, D. Zwicker, Cavitation controls droplet sizes in elastic media. *Proc. Natl. Acad. Sci. U.S.A.* **118**, e2102014118 (2021).
61. C. Pérez-González *et al.*, Active wetting of epithelial tissues. *Nat. Phys.* **15**, 79–88 (2019).
62. D. T. Wasan, A. D. Nikolov, Spreading of nanofluids on solids. *Nature* **423**, 156–159 (2003).
63. A. A. Pahlavan, L. Yang, C. D. Bain, H. A. Stone, Evaporation of binary-mixture liquid droplets: The formation of picoliter pancakelike shapes. *Phys. Rev. Lett.* **127**, 024501 (2021).
64. H. Wang, Y. Liu, Z. Chen, L. Sun, Y. Zhao, Anisotropic structural color particles from colloidal phase separation. *Sci. Adv.* **6**, eaay1438 (2020).
65. Q. Ma *et al.*, Cell-inspired all-aqueous microfluidics: From intracellular liquid–liquid phase separation toward advanced biomaterials. *Adv. Sci. (Weinh.)* **7**, 1903359 (2020).
66. S. U. Setru *et al.*, A hydrodynamic instability drives protein droplet formation on microtubules to nucleate branches. *Nat. Phys.* **17**, 493–498 (2021).
67. T. J. Böddeker *et al.*, Non-specific adhesive forces between filaments and membraneless organelles. *Nat. Phys.* **18**, 571–578 (2022).
68. O. Ramírez-Soto, S. Karpitschka, Taylor dispersion in thin liquid films of volatile mixtures: A quantitative model for Marangoni contraction. *Phys. Rev. Fluids* **7**, L022001 (2022).
69. E. Kadivar, C. Bahr, H. Stark, Crossover in the wetting behavior at surfactant-laden liquid-crystal-water interfaces: Experiment and theory. *Phys. Rev. E Stat. Nonlin. Soft Matter Phys.* **75**, 061711 (2007).